Journal of CO2 Utilization 83 (2024) 102804

Contents lists available at ScienceDirect

Journal of CO2 Utilization

journal homepage: www.elsevier.com/locate/jcou

Insight on Zn-Al LDH as electrocatalyst for CO_2 reduction reaction: An *in-situ* ATR-IR study

Margherita Cavallo [a], Melodj Dosa [a], Ryosuke Nakazato [b], Natale Gabriele Porcaro [a], Matteo Signorile [a], Matthias Quintelier [d], Joke Hadermann [d], Silvia Bordiga [a], Nataly Carolina Rosero-Navarro [b,c], Kiyoharu Tadanaga [b], Valentina Crocellà [a], Francesca Bonino [a,*]

[a] Department of Chemistry, NIS and INSTM Reference Centers, Università di Torino, Via Quarello 15/A, Torino 10135, Italy
[b] Division of Applied Chemistry, Faculty of Engineering, Hokkaido University, Sapporo, Hokkaido 060-8628, Japan
[c] Instituto de Cerámica y Vidrio, ICV-CSIC, Madrid 28049, Spain
[d] EMAT, Department of Physics, University of Antwerp, Antwerp 2020, Belgium

ARTICLE INFO

Keywords:
In-situ ATR-IR spectroscopy
Layered Double Hydroxide
CO_2 reduction reaction
Electrocatalysis

ABSTRACT

Electrochemical reduction of CO_2 (CO2RR) is expected to play a key role among the various strategies being explored to limit global warming. In this scenario, Layered Double Hydroxides (LDHs) are emerging as a promising class of electrocatalysts to replace the most used noble metals. In this work three Zn-Al LDH with different Zn^{2+}/Al^{3+} ratio were synthesized and characterized by means of XRD, STEM-EDX and HR-TEM. Their suitability for CO2RR to CO was assessed by means of a custom-made three-compartment cell, showing an increase in CO selectivity by decreasing the Zn^{2+}/Al^{3+} ratio. The CO_2 interaction with the samples was firstly characterized by means of volumetric adsorption measurements, exhibiting an increase in capture capacity by decreasing the Zn^{2+}/Al^{3+} ratio. The evolution of the samples in interaction with a CO_2-saturated liquid flow was then deeply investigated by means of *in-situ* ATR-IR spectroscopy. The samples displayed a different evolution in the vibrational region of the carbonate-like species (1800–1200 cm^{-1}). To better discriminate the different carbonate cyclohexane was also employed. A definitive assignment of the main IR bands of the carbonate was carried out by studying the spectral behavior of the different bands observed in the ATR-IR experiments and by comparing these results with the existing literature. Interestingly, Zn-Al 1:2 LDH, the most efficient electrocatalyst for CO2RR, is also the sole sample exhibiting a higher monodentate to total bidentate carbonates ratio, suggesting that the existence of a higher content of low coordination oxygen anions with stronger basic character can influence the final catalytic activity.

1. Introduction

In the last centuries, there has been a steady increase in carbon dioxide (CO_2) emissions due to anthropogenic activities. Atmospheric CO_2 concentrations have risen from 277 ppm in 1750 to 410 ppm in 2019, leading to an increase in the global temperature of more than 1 °C [1]. Among the various strategies being explored to limit global warming, Carbon Capture and Utilization (CCU) technologies are expected to play a crucial role, offering the potential not only to mitigate emissions, but also to convert CO_2 into a source of fuels and chemicals [2,3].

Various methods, including thermochemical, biological, photochemical and electrochemical conversion, have been investigated to reduce CO_2 [4]. The thermochemical route, despite being the most widely used and the most mature technology, requires also the highest heat and pressures [5]. On the other hand, biological and photochemical systems minimize the energetic impact, but the efficiency and selectivity are usually far from large-scale application [6]. In this context, the electrochemical reduction of CO_2 (CO2RR) presents important advantages, such as easy control of the reaction product and rates by changing the overpotential, mild reaction temperatures and easy separation of the reaction products, by placing the electrodes into individual chambers [7,8]. Depending on the catalyst and other parameters involved in the reaction, the electrochemical reduction of CO_2 can lead to the formation of various products such as formic acid (HCOOH), methane (CH_4), methanol (CH_3OH), ethylene (C_2H_4), ethanol (CH_3CH_2OH) and carbon monoxide (CO) [8]. Among them, CO is of great interest as it is the

* Corresponding author.
E-mail address: francesca.bonino@unito.it (F. Bonino).

https://doi.org/10.1016/j.jcou.2024.102804
Received 16 February 2024; Received in revised form 3 May 2024; Accepted 10 May 2024
Available online 19 May 2024

starting point to produce various hydrocarbons and an intermediate for further reduced products [9,10]. The most active electrocatalysts for the selective reduction of CO_2 to CO are Au and Ag, but their high cost and scarcity are drawing attention to the study of lower-cost systems using earth-abundant elements [11,12]. In recent years, layered double hydroxides (LDHs) have been widely studied as promising electrocatalysts, due to their interesting characteristics such as low cost, easy synthesis procedure, tunability of composition, good ionic conductivity, and high alkaline tolerance [13–15]. LDHs or hydrotalcites (HT) structures are characterized by layers of divalent and trivalent cations in octahedral coordination with hydroxyl ions, causing an overall positive charge density which is balanced by the presence of divalent anions which are present in the interlayer along with water. The general molecular formula is $[M(II)_{(1-x)}+)M(III)_x+(OH)_2]^{x+}[A^{n-}_{x/n}]$ mH_2O where M(II) and M (III) are respectively the divalent and the trivalent cations, A^{n-} is the anions and x is the fraction of M(III) cation (x = M(III) / (M(II) + M(III)). As the temperature is increased, the layered structure slowly collapses to form a mixed oxide configuration (layered double oxide, LDO) and finally a spinel structure. Interestingly, the LDH exhibits a memory effect which allows the original structure to be easily restored by rehydrating the LDO [16]. This feature, together with the versatility of the structures that can be easily modified by changing the metals and the interlayer anions, contribute to making this material suitable for a variety of applications in addition to electrocatalysis [17].

Over the years, LDHs with different metal compositions were proven to be potential electrolytes for alkaline type fuel cells thanks to their high ionic conductivity [18,19] as well as promising catalysts for CO_2 photoreduction [20] and an alternative to IrO_2 and RuO_2 as electrocatalysts for oxygen evolution reaction (OER) [21–24]. More recently, Cu-Al LDH and Cu-Mg-Al LDH were employed for CO_2 reduction to CO/HCOOH and CH_3COOH respectively [25,26]. The potential use of LDHs for the selective reduction of CO_2 to CO was recently evaluated by comparing three Zn-Al LDHs with increasing Zn^{2+}/Al^{3+} molar ratios (2:1, 3:1 and 4:1) [27]. The Zn-Al 2:1 LDH was proven to be a promising electrocatalyst for CO2RR showing a CO selectivity of 77% at 1.4 V vs. RHE in a potassium bicarbonate ($KHCO_3$) solution. Afterward, keeping the M^{2+}/M^{3+} molar ratio constant, the activity of Ni-Al, Ni-Fe and Zn-Al LDHs was compared showing for the latter one the highest CO evolution [28].

Although many studies have been carried out over the years on the composition and preparation of the electrocatalyst, modifications in the electrolyte, variations of the cell design with the ultimate aim of improving the electrochemical activity, little attention has been paid to the detailed characterization of the active sites present in the electrocatalysts and to a deep understanding of the interfacial region. Since the electrochemical reactions take place at the interface between the catalysts and the electrolytic solutions, a deep understanding of the initial structure and of the species formed at the surface is expected to play a central role in the comprehension of the reaction mechanism [29]. Many papers investigated the type, and the strength of the different basic sites present in LDHs by means of IR spectroscopy, distinguishing between the different carbonate-like species formed upon CO_2 interaction [30–34]. However, the pre-treatment of the sample, which modifies the original LDH structure, and the measurement conditions usually employed, lead to a characterisation of the materials in a state far away from their real application. On the other hand, the experimental techniques able to couple electrochemical and IR spectroscopic, which have been widely employed recently [29], still have some limitations in application, in particular: (i) ensuring good conductivity of the system in poorly conducting samples without affecting the actual performance of the catalyst (ii) difficulty in reproducing the results obtain ed in classical electrochemical cells.

Attenuated Total Reflection Infrared Spectroscopy (ATR-IR) demonstrated over the years to be particularly suitable for the study of samples interacting with a liquid interface [35–38]. The strength of this technique compared to other spectroscopic approaches lies in some key features such as (i) the intrinsically low penetration depth of the IR beam in the sample allows investigating mostly the interfacial region, thus largely avoiding the contribution of the bare liquid phase to the spectrum (ii) the possibility to optimize the signal to noise ratio with multiple reflections [39].

In the present study, three different as-synthesized Zn-Al LDHs having progressively lower M^{2+}/M^{3+} molar ratios (2, 1 and 0.5) were electrochemically tested for CO2RR to CO. The interaction of a CO_2-saturated liquid flow with the three samples was deeply investigated by means of ATR-IR spectroscopy to disclose the existence of different active sites and correlate them with the catalytic activities of the different LDHs.

2. Material and methods

2.1. Materials

Zinc nitrate hexahydrate ($Zn(NO_3)_2{\cdot}6\ H_2O$, 99.0%), aluminum nitrate nonahydrate ($Al(NO_3)_3{\cdot}9\ H_2O$, 98.0%), sodium carbonate (Na_2CO_3, 99.8%), potassium bicarbonate ($KHCO_3$, > 99.5%), and sodium hydroxide (NaOH, 97.0%) were purchased from FUJIFILM WAKO PURE CHEMICAL Co. Ethanol (EtOH, > 99.5%) was purchased from Kanto Chemical Co., Inc. Water was purified by a distilled water production system (SHIMIZU SCIENTIFIC INSTRUMENTS MFG Co., Ltd.). An anion exchange membrane (AHA) was purchased from ASTOM Corp. CO_2 gas (>99.5%) was purchased from TAIYO NIPPON SANSO HOKKAIDO Corp. All other solvent and chemicals in reagent grade were purchased and were used without further purification. CO_2 gas (99.995%) was purchased by SAPIO group SRL for the volumetric and spectroscopic measurements, N_2 gas (99.999%) was purchased by SAPIO group SRL and C_6H_{12} ACS reagent, ≥99%, provided by Sigma-Aldrich were used for spectroscopic measurements.

2.2. Synthetic procedure and fundamental characterization

Zn-Al LDHs (Zn-Al 1:2, Zn-Al 1:1, and Zn-Al 2:1) were prepared using a facile and traditional coprecipitation process [27,28]. $Zn(NO_3)_2{\cdot}6\ H_2O$ and $Al(NO_3)_3{\cdot}9\ H_2O$ were dissolved in deionized water with Zn^{2+}/Al^{3+} = 2.0, 1.0, 0.50 mol%. The mixture was dropped into 0.30 M Na_2CO_3 solution with stirring at 353 K. The drop rate was adjusted to 2 mL min^{-1} by using a syringe pump (SPE-1, AS ONE Corp.). The pH of the reaction mixture was adjusted to 10 by adding 2.0 M aqueous NaOH solution with a pH meter (pH700, Eutech Instruments Pte. Ltd.). The obtained solution was aged at room temperature for 24 h. The resulting white precipitate was filtered, washed with distilled water, and dried at 323 K for 24 h. The products were labeled as Zn-Al 1:2, Zn-Al 1:1, and Zn-Al 2:1, corresponding to the starting composition ratio of Zn and Al.

The products were characterized by powder X-ray diffraction (XRD) to identify the crystalline phase. XRD patterns (CuKα) were taken using an XRD diffractometer (Mini Flex 600, Rigaku Corp.).

To check the morphology and the experimental Zn:Al ratio STEM-EDX measurements were performed. The samples were dissolved in ethanol and sonicated for 10 minutes before being drop-casted on a standard TEM grid. STEM-EDX experiments were performed using a ThermoFisher Osiris microscope operated at 200 kV and equipped with a SuperX detector. BF-TEM experiments were performed using a ThermoFisher Tecnai G2 microscope operated at 200 kV and equipped with a Gatan US1000XP CCD camera. HR-TEM images were taken using an image corrected ThermoFisher Titan microscope operated at 300 kV and equipped with a Gatan K2 direct electron detector.

2.3. Electrocatalytic CO2RR experiment

On the three synthesised samples, the electrocatalytic CO2RR experiments were carried out by using a custom-made three-electrode setup composed of a three-compartment cell (see Figure S1) [28]. The

cathodic and anodic compartments were separated by a piece of the anion exchange membrane to avoid the unexpected influence of the oxidation reaction taking place on the counter electrode. The LDH-loaded gas-diffusion electrode (GDE) and a platinum mesh electrode (35 × 25 mm, LAKE SHORE CRVOTRONICS Inc.) were used as working and counter electrodes, respectively. The LDH-loaded GDE was prepared by simple drop-casting of the catalyst ink on a gas-diffusion layer (GDL: Sigracet 36BB, SGL CARBON JAPAN Ltd.). The catalyst inks were prepared by mixing 4 mg of LDH ground for 5 min with 1 mg of the conductive aid (carbon black: Vulcan XC72, CABOT Corp.) and 30 μL of the binder (Nafion solution, SIGMA-ALDRICH Co. LLC) in 570 μL of ethanol and sonicating for 10 min. The catalyst ink was drop-casted to the GDL on a hot plate pre-heated at 353 K. The ink coating area was 1.89 cm^2, whose shape was a 1.55 cm diameter circle and the loading level of the LDH was 2.1 mg cm^{-2}. The LDH-loaded GDE was further dried at 353 K for at least 30 min to remove the solvents. Ag/AgCl (3.0 M KCl, BAS Inc.) electrode was used as a reference. An aqueous solution (0.10 M) of $KHCO_3$ was used as an electrolyte. The CO_2 gas flowed with a 50 mL min^{-1} flow rate and 0.10 MPa inlet pressure to the cathodic compartment, while the solution in the reference electrode compartment was stirred at 600 rpm with a PTFE stirring bar. Under the above conditions, CO_2 electrolysis for 10 min was performed by applying a voltage with an electrochemical analyser (IviumStat, IVIUM TECHNOLOGIES B.V.). Gas-phase products were detected by gas chromatography techniques (GC-2014, SHIMADZU Corp.; carrier gas: nitrogen, flow rate: 10 mL min^{-1}, pressure: 53.2 kPa, vaporization chamber temperature: 393 K). For the detection of hydrogen (H_2), Molecular Sieve 5 A (GL SCIENCES Inc.; column temperature: 323 K, injected sample volume: 1 mL) and a thermal conductivity detector (TCD, SHIMADZU Corp.; detector temperature: 393 K) were used. For the detection of CO and gaseous hydrocarbons, PoraPak N (GL SCIENCES Inc.; column temperature: 323 K, injected sample volume: 1 mL) for a flame ionization detector (FID, SHIMADZU Corp.; detector temperature: 393 K) were used. Electrode potentials in the study were converted to the reversible hydrogen electrode (RHE) according to the following equation (Eq. 1):

$$E_{RHE} = E_{Ag/AgCl} + 0.222V + 0.059 \quad xpH \tag{1}$$

All potentials and voltages in this work were evaluated without IR calibration. The Faradaic efficiency (*FE*) for CO and H_2 was calculated based on the Eq. 2 [40]:

$$\mathrm{FE} = \frac{2\mathrm{Vp\ rF}}{\mathrm{IRT}} \tag{2}$$

Where *V* was the volume concentration of CO or H_2 in the produced gas from the reaction cell. *I* (mA) was the average current during the reaction, and *r* was the CO_2 flow rate ($m^3\ s^{-1}$) at ambient temperature and pressure. For the other constants in the formula, *p* was 1.013×10^5 Pa, *F* was 96485 C mol^{-1}, *R* was 8.3145 J $mol^{-1}\ K^{-1}$, and *T* was 298 K.

2.4. Advanced Characterization

A deep spectroscopical investigation was performed on the three Zn-Al LDHs to identify possible differences in active sites on the different samples.

A first preliminary investigation of the materials affinity for CO_2 was performed by evaluating the CO_2 capture capacity, by collecting adsorption/desorption isotherms. The measurements were performed at 308 K using a Micromeritics 3Flex sorption analyzer. The temperature was kept constant thanks to a Thermoelectric Cooled Dewar (ISO Controller) provided by Micromeritics. This measurement temperature was chosen due to the better temperature stability observed with this setup under these conditions. The samples were previously pre-treated under vacuum at 353 K for 4 h. This activation temperature was carefully chosen to preserve the LDH original structure, by examining the variable temperature X-ray diffraction (VT-XRD) pattern of the Zn-Al 2:1sample. The VT-XRD was performed between room temperature and 723 K using a SmartLab diffractometer (Rigaku, CuK1, λ= 1.541Å). The temperature ramp was set at 5 K min^{-1} and the diffractograms were collected in isothermal condition every 10 K. Raman spectra were collected on a Renishaw inVia Raman microscope spectrometer. A diode laser emitting at 785 nm was used while photons scattered by the sample were dispersed by a 1200 lines/mm grating monochromator and simultaneously collected on a CCD camera. The collection optic was set at 50X objective, and the spectral collection consisted of 10 acquisitions, each of 10 s. The spectra of the three LDH samples were obtained by summing up three different spectra.

In-situ ATR-IR measurements were performed with a Bruker Invenio Fourier transform spectrometer to investigate the effect of the interaction of CO_2 with the LDH samples. The spectrometer is equipped with a MCT cryo-detector (Mercury Cadmium Telluride) which operates at liquid nitrogen temperature (~77 K). During the test, each collected spectrum consists of an average of 32 scans (64 for the background spectrum). The ATR-IR measurements were carried out using a commercial horizontal ATR mirror unit and cell (HATR, Horizontal ATR accessory provided by Pike Technologies) equipped with an AMTIR single crystal (internal reflection element 80×10×4 mm, 45°, Specac). Prior to each measurement, LDH samples were suspended in deionized H_2O (~10 mg per 0.5 mL), deposited on the crystal and dried overnight at room temperature. The ATR-IR spectra of the dried samples were collected before each experiment. The structural interlayer carbonates were identified, and the underlying area was used to normalize the following LDH spectra.

The ATR cell was then flushed with liquid H_2O saturated with N_2 which was supplied through a mass flow controller with a flow rate of 15 mL min^{-1}·H_2O and N_2 were circulated over the deposited LDH at room temperature for 30 minutes to verify the stability of the sample deposition. The circulation was controlled through a peristaltic pump operated at 2.0 mL min^{-1}. The inlet gas was then switched to CO_2 and a CO_2-saturated liquid H_2O flow was circulated over the sample for another 30 minutes (a schematic representation of the setup is reported in Scheme 1).

The same experiment was repeated with cyclohexane instead of H_2O to further characterize the sample. Based on those results, a band fitting of the carbonates-like species formed on the LDH structure was performed by means of the FIT routine by Bruker, which allows the interactive search for the best fit to the examined experimental spectral segment based on several spectral components imposed by the operator. Once the spectral position and all the major spectral parameters (half-bandwidth, percent of Gaussian profile) have been fixed, the remaining ones were allowed to float freely. Lastly, the carbonates evolution in time was studied by making a fitting of the carbonates originated from the CO_2-saturated H_2O flow at 0,7.5,15, 22.5, 30 minutes. The underlying area of each couple of carbonates was calculated and reported in histograms.

3. Results and discussion

XRD patterns were first collected to check the crystalline structure of the synthesized LDHs (Figure S2). For all the samples, the (003) and (006) plane reflections, characteristic of the layered structure, were observed and were assigned to the previously reported XRD pattern of Zn-Al LDH with carbonate (CO_3^{2-}) as interlayer anions [41], without other impurity peaks.

In Fig. 1 BFTEM, HRTEM and STEM-EDX maps are shown. The BF TEM analysis (Fig. 1a-c) revealed the typical hexagonal particles morphology in all LDH samples. The three samples show differences in particle size and mean particle thickness, HR-TEM also revealed variations in the mean basal spacing (see Table S1 for the values).

STEM-EDX elemental analysis (Fig. 1g-i) yielded mean Zn:Al ratios of 1.96(25), 1.56(20), and 1.19(38) for Zn-Al 2:1, Zn-Al 1:1, and Zn-Al 1:2,

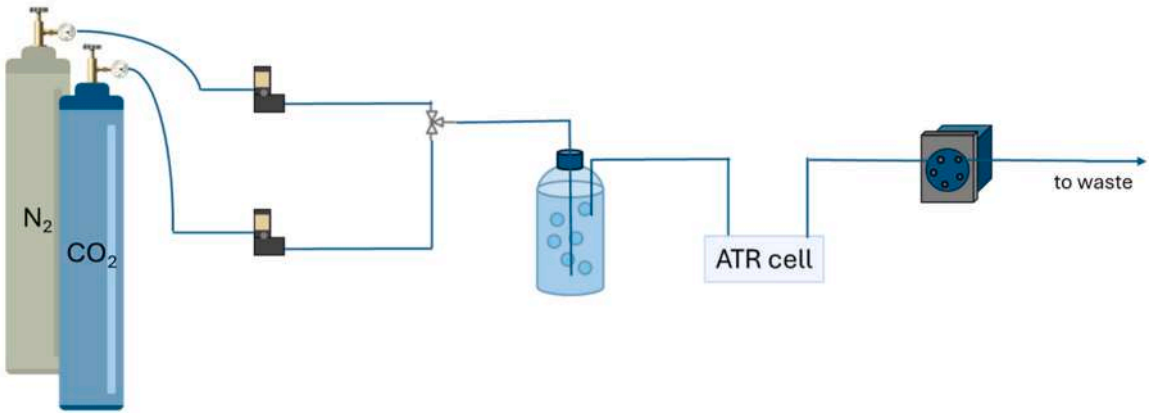

Scheme 1. Schematic representation of the set-up used during the in-situ ATR-IR measurement.

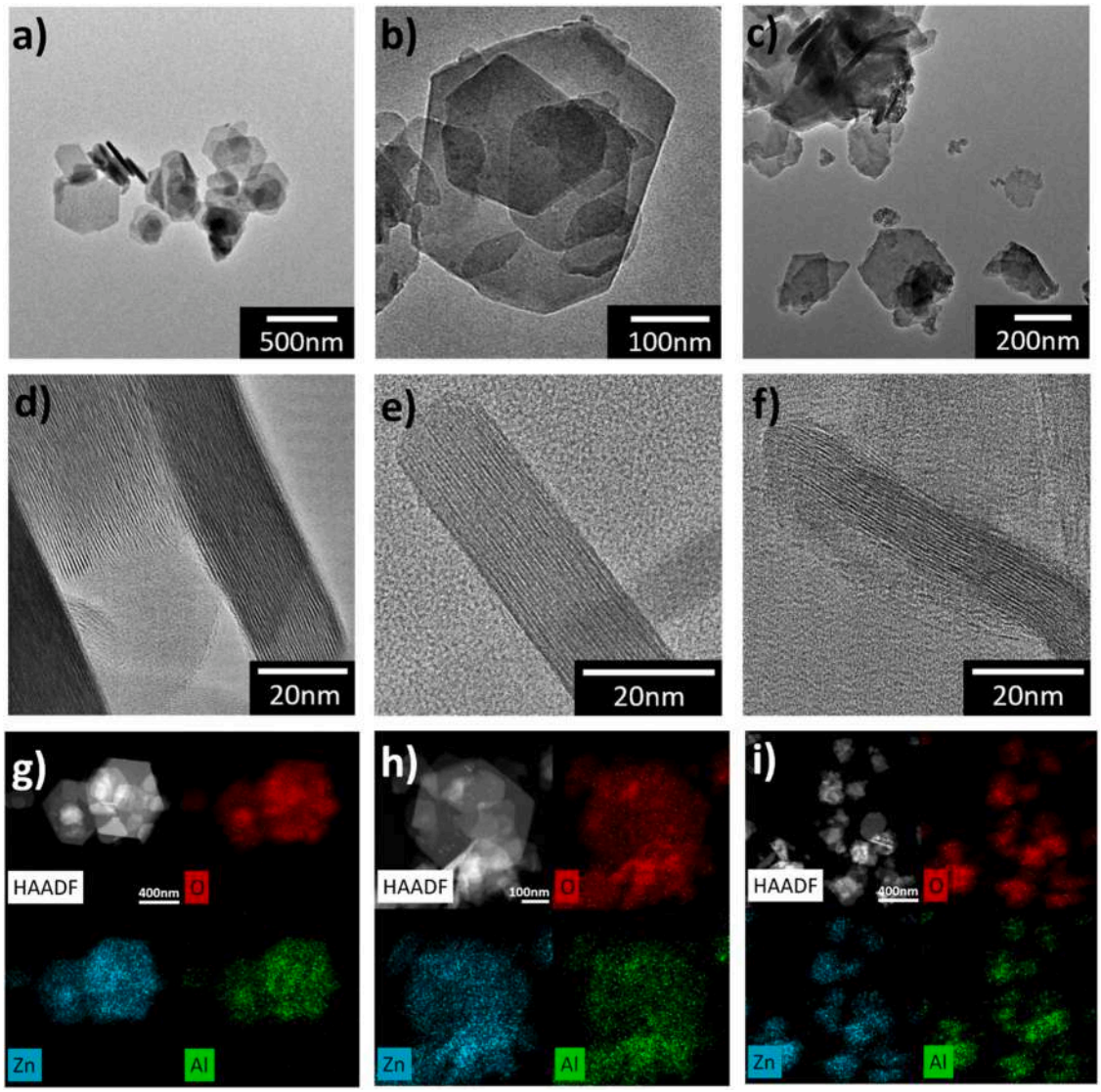

Fig. 1. (top) BF-TEM (middle) HR-TEM images and (bottom) HAADF-STEM elemental maps of Zn-Al 2:1 (a,d,g), Zn-Al 1:1 (b,e,h) and Zn-Al 1:2 (c,f,i). All maps are given in counts.

respectively. In the Zn-Al 1:1 and Zn-Al 1:2 samples there were also smaller particles present that contained only aluminum. This could explain the deviation of the measured mean Zn:Al ratio from the expected value. Considering that no impurity peak was observed in the XRD pattern, the particles containing only aluminum were ascribed to amorphous alumina.

The potential application of Zn-Al LDHs as electrocatalysts for CO2RR to CO was then evaluated by means of a three-compartment cell (see Figure S1). The electrocatalytic CO2RR was performed at the applied potentials of −0.60 to −1.40 V vs. RHE in 0.1 M aqueous $KHCO_3$ solution as a typical electrolyte. The applied potential dependence of current density (*j*) and Faradaic efficiency (*FE*) are shown in Fig. 2.

Fig. 2 shows that the catalytic currents were observed and increased with more negative applied potentials in all the samples. The main gaseous products for all the Zn-Al LDHs were CO and H_2, and the partial current densities of CO evolution tended to be larger in the case of Zn-Al 1:1 and Zn-Al 1:2 than in the case of Zn-Al 2:1 while the total current density and the partial current density of H_2 evolution were larger in the order Zn-Al 2:1 > Zn-Al 1:1 > Zn-Al 1:2, thus H_2 evolution tended to be suppressed for smaller Zn/Al ratios. The suppression of H_2 evolution mainly contributed to the increase of *FE* of CO evolution (FE_{CO}) with decreasing Zn/Al ratios, which were 11, 37, and 40% at −1.4 V vs. RHE for Zn-Al 2:1, Zn-Al 1:1, and Zn-Al 1:2, respectively. On the other hand, the *FE* of H_2 evolution (FE_{H2}) decreased with decreasing Zn/Al ratios, which were 73, 48, and 42% at −1.4 V vs. RHE for Zn-Al 2:1, Zn-Al 1:1, and Zn-Al 1:2, respectively. These results show a progressive suppression of H_2 evolution in favor of CO by decreasing the Zn/Al ratio, reaching the best performances for Zn-Al 1:2. Additionally, the STEM-EDX elemental analysis suggests that amorphous alumina detected in Zn-Al 1:1 and Zn-Al 1:2 could contribute to the suppression of H_2 and to the parallel promotion of CO evolution. Even if alumina itself is basically inert to electrochemical reactions, [42,43] low alumina content in oxide matrices or as a catalyst surface modifier has proven to be also beneficial since tuned properties such as active chemical sites enhancement and oxidation capacity can be achieved [42–46]. In this sense, stronger oxidation capacity could accelerate the production of reactive oxygen species (O^{2-}, O_2^- and O^-.) [46]. Therefore, amorphous alumina contained in Zn-Al 1:1 and Zn-Al 1:2 could also contribute in the enhancement of CO evolution

The three LDHs were then deeply characterized to investigate possible differences in their active sites.

The CO_2 adsorption capacities of the Zn-Al LDHs was investigated by collecting volumetric CO_2 adsorption isotherms at 308 K (Figure S3). Prior to the measurements, the samples were activated at 353 K for 4 h in vacuum. To prove that the original LDH structure is still preserved under those activation conditions, a VT-XRD experiment was performed on the Zn-Al 2:1 sample (Figure S4). The reflections associated to the LDH structure disappeared between 373 and 423 K. However, since the activation prior to the volumetric measurements is performed under more severe conditions (i.e., in vacuum and not under inert gas flow), the selected safety temperature for the pretreatment was lower than 373 K.

Although the overall CO_2 uptake at 308 K is low (< 0.5 mmol/g) for all samples, the three LDHs exhibit the following CO_2 adsorption trend: Zn-Al 1:2 >> Zn-Al 1:1 > Zn-Al 2:1. Even if the volumetric measurements are performed with pure CO_2 in gas phase (i.e. far from the real catalytic conditions), they provide a first insight into the different affinity of materials for CO_2. ... It is worth noting that Zn-Al 1:2, displaying the best catalytic performances, has also the highest CO_2 capture capacity. This behavior suggests that a peculiar CO_2 adsorption

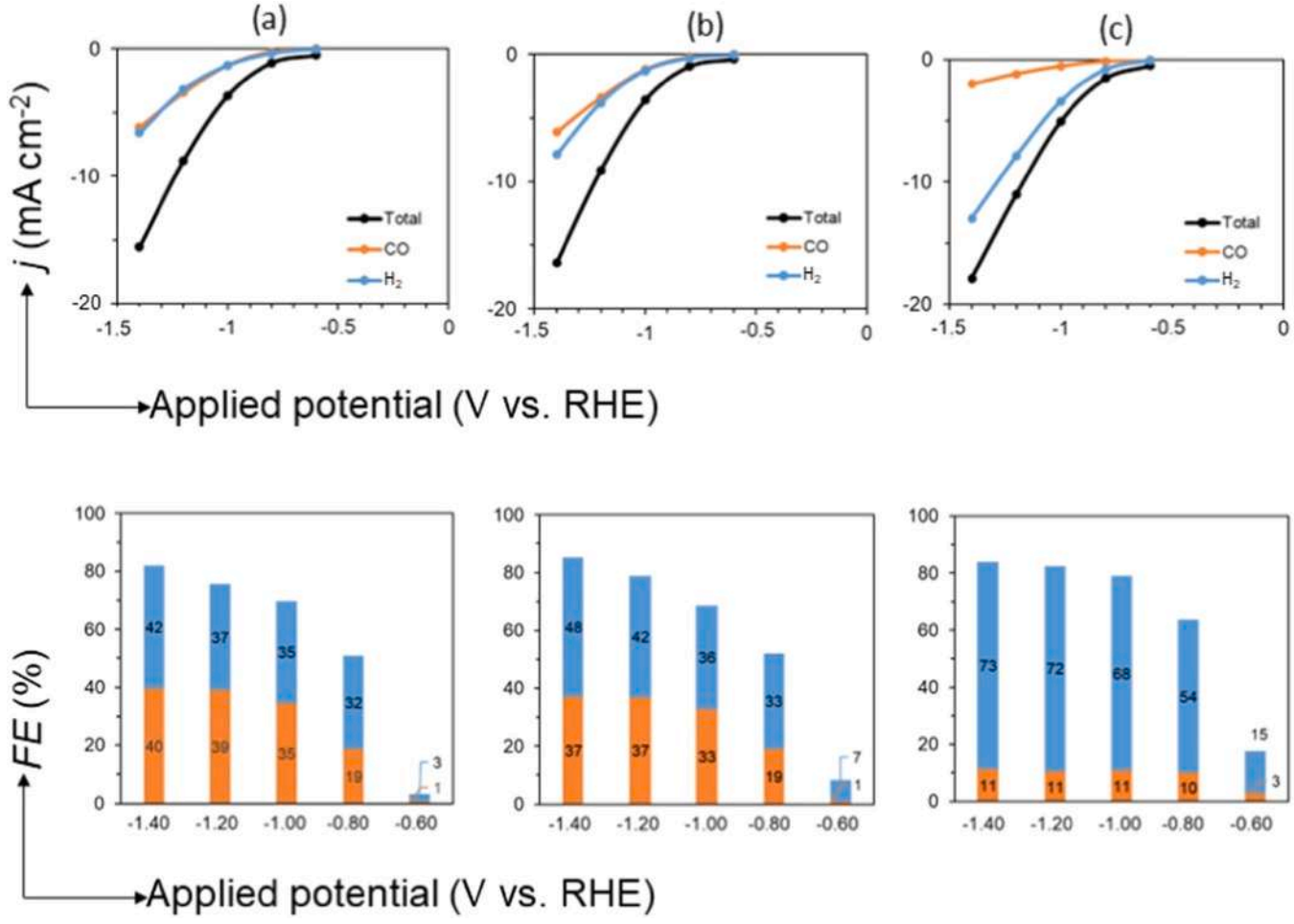

Fig. 2. Applied potential dependence of current density (j, upper row figures) and Faradaic efficiency (FE, lower row figures; orange bar: CO, blue bar: H_2) for CO2RR in 0.10 M aqueous $KHCO_3$ solution with (a) Zn-Al 1:2, (b) Zn-Al 1:1, and (c) Zn-Al 2:1.

mechanism occurs in Zn-Al 1:2 sample. Therefore, a further investigation of the CO_2 interaction mechanism in conditions closer to the electrocatalytic ones was carried out by means of in-situ ATR-IR spectroscopy.

To have a clear overview of the different species involved, the spectra of the dried depositions (i.e. obtained on the ATR-IR crystal after solvent evaporation, as reported in the experimental section) were first collected and analyzed (Fig. 3).

All the samples exhibit a broad band at high wavenumbers (3900–2500 cm^{-1}) ascribable to the hydroxyl stretching vibrations. In this spectral region three main contributions could be identified: i) the -OH stretching vibration of structural M-OH (M = Zn or Al) species (3500–3400 cm^{-1}); ii) OH stretching vibrations of the interlayer H_2O molecules (3300–3100 cm^{-1}); and iii) OH stretching vibrations perturbed by the bridging mode of CO_3^{2-} - H_2O species located in the interlayer (3050–2950 cm^{-1}) [47,48].

In the low frequency region (1000–650 cm^{-1}), another broad band can be identified in all the LDH samples. This signal results from the overlapping of the ν_2 out of plane stretching mode of structural interlayer CO_3^{2-} carbonate anions (at ~860 cm^{-1}) and of the lattice HO-M-OH and M-OH (450–800 cm^{-1}) vibrations [49,50].

Lastly, in the intermediate spectral region (1800–1200 cm^{-1}), a band at 1640 cm^{-1}, attributed to the bending vibrations of the structural interlayer water molecules and physiosorbed water, and a band at about 1400 cm^{-1}, corresponding to the asymmetric stretching ν_3 mode of the structural interlayer CO_3^{2-}, were observed [51]. Interestingly, there is lower wavenumber component (~1365 cm^{-1}) in this last band. As reported by Labajos and al., [52] the interaction of the carbonate ions with water in the interlayer is responsible for a decrease in symmetry compared to the free carbonate ion leading to a splitting of the ν_3 asymmetric stretching bands. The different components just described are highlighted in the band fitting of the 1800–1200 cm^{-1} region, shown in Figure S5. A further proof of this phenomenon is the clear appearance of the ν_1 symmetric stretching band at 1060 cm^{-1} in the spectrum of Zn-Al 1:2. This signal is usually IR inactive, but it could be activated by the symmetry change of the interlayer carbonates.

The other bands in the 1550–1480 cm^{-1} range originate from the formation of surface (non-structural) carbonate-like species, due to the exposure of the material to the atmospheric CO_2. These signals could be removed by performing a high temperature pre-treatment, but as mentioned above, the original LDH structure is only preserved if the temperature does not exceed 373 K.

The mid-IR spectral range of the three samples perfectly match with the Raman spectra (Table S2 and Figure S6), where the ν_1 CO_3^{2-} symmetric stretching is clearly visible at 1061 cm^{-1}, while the other two less intense Raman-active carbonates vibrations at 680 cm^{-1} (ν_4 in-plane deformation) and 1415 cm^{-1} (ν_3 asymmetric stretching) were not observed due to their weak nature and the partial fluorescence of the samples [51]. At lower wavenumbers, two narrow bands were observed at 553 cm^{-1} and at 480 cm^{-1}, attributed to the Al-O-Zn and Al-O-Al

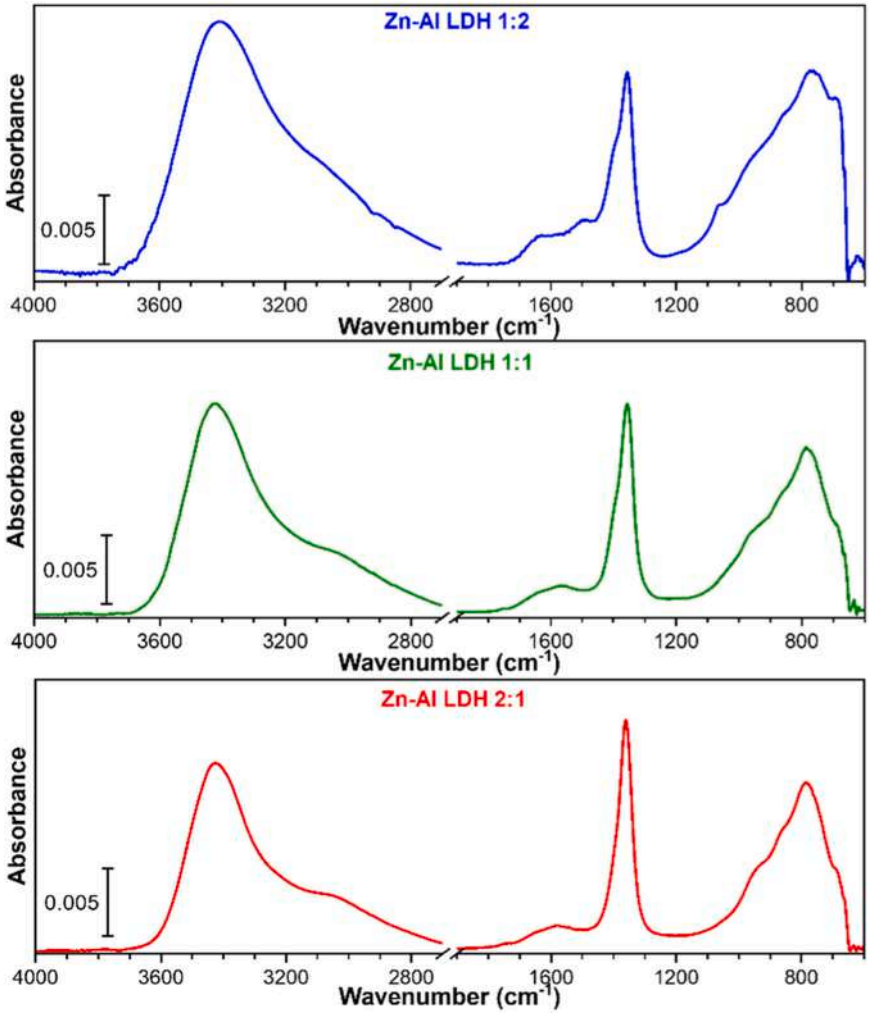

Fig. 3. ATR-IR spectra of the dried samples of Zn-Al 1:2 (blue curve), Zn-Al 1:1 (green) and Zn-Al 2:1 (red curve). The spectra were normalized by the underlying area of the structural interlayer carbonates (Fig. S5).

vibrational modes, respectively, [53]. The signal at 153 cm^{-1}, previously observed by Palmer et al., can be assigned to vibration modes involving the hydrotalcite OH units and the water molecules in the interlayer [53]. At higher wavenumbers, the florescence is preventing a clear identification of the main components.

After investigating the main bands present in the different spectra of dried Zn-Al LDHs depositions, the interaction of the samples with a CO_2-saturated H_2O flow was examined by means of ATR-IR spectroscopy, following the methodology described in Section 2.2 (Fig. 4a-c).

The interaction of CO_2-saturated liquid H_2O leads to the appearance of a variety of signals in the 1800–1200 cm^{-1} spectral region, usually associated with carbonate-like species originating from the interaction of CO_2 with the basic LDH sites [51]. As previously mentioned, when the symmetry of the free carbonate ions is lowered, the original ν_3 asymmetric CO_3^{2-} stretching band at around 1415 cm^{-1} present in the LDHs spectra (Fig. 4) splits in two distinct components (the symmetric ν_{3sym} and the asymmetric ν_{3asym} vibrations). Depending on the type and strength of the surface sites, different carbonate-like species are formed resulting in a complex carbonate evolution spectral profile.

The spectrum of Zn-Al 1:2 shows a rapid increase of the bands at ~1340 cm^{-1}, followed by a gradual increment of the signal at 1520 cm^{-1}. This latter band probably overlaps to another signal at lower wavenumbers (approximately 1450 cm^{-1}), rising with a similar trend. Additionally, the broadness of the band related to the HOH bending vibrations at 1640 cm^{-1} also suggests the existence of other spectral components superimposed at higher wavenumbers. The spectra collected at higher CO_2 coverage (colored curves) display an unusual minimum at 1363 cm^{-1}, which further complicates the identification of the different components, especially for Zn-Al 1:1 and Zn-Al 2:1 LDHs. This downwards band will be discussed in detail later on.

The Zn-Al 1:1 sample shows, similarly to Zn-Al 1:2, a first increase of the 1340 cm^{-1} band followed by of the rise of a broad band in the 1580 and 1400 cm^{-1} spectral region. Unfortunately, this sample exhibits an important minimum at 1363 cm^{-1} which partially hides a probable second component at around 1450 cm^{-1} and leads to a difficult identification of the real maxima of the different spectral components. For Zn-Al 1:1 and even more for Zn-Al 2:1, the carbonates evolution seems to be lower compared to Zn-Al 1:2, especially for the bands between 1580 and 1400 cm^{-1} which are nearly absent for Zn-Al 2:1. Indeed, for this sample the prevalent band is the HOH bending at 1640 cm^{-1}, together with the presence of the minimum at 1363 cm^{-1}.

Notably, all samples show a decrease in intensity at 1363 cm^{-1}, leading to the appearance of negative bands for Zn-Al 1:1 and Zn-Al 2:1. Since the vibrational frequency of this negative signal coincides with that of the structural interlayer carbonates (see comparison in Figure S7), it is likely due to a loss of deposition by the crystal, generated by the CO_2-saturated H_2O flow. To minimize the risk of deposition loss and to better appreciate the carbonates bands hidden by the presence of

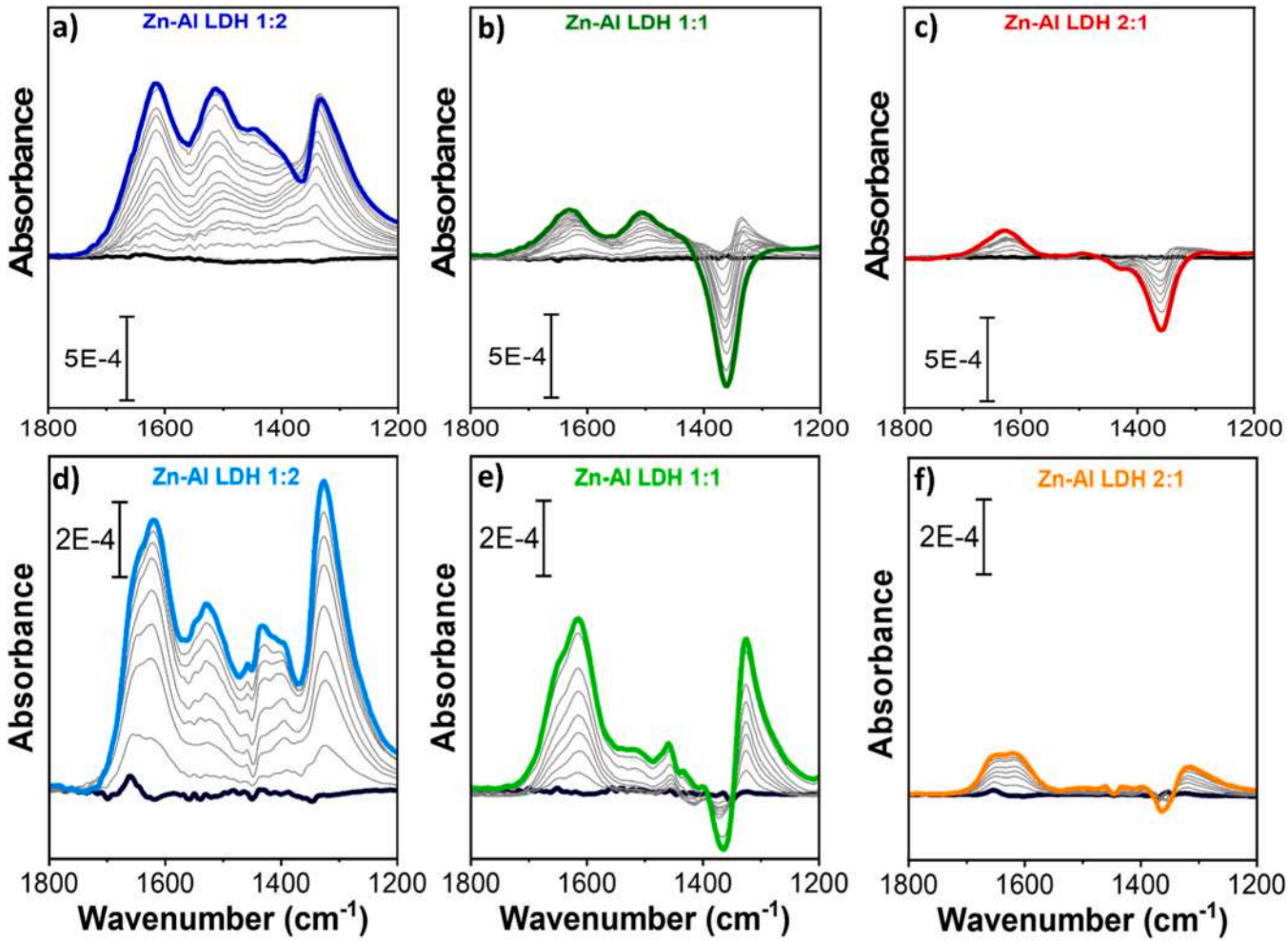

Fig. 4. *In-situ* ATR-IR spectra in the carbonate-like region (1800–1200 cm^{-1}) of Zn-Al 1:2 (a, d), Zn-Al 1:1 (b, e) and Zn-Al 2:1 (c, f) under a CO_2-saturated H_2O flow (a, b and c) and under a CO_2-saturated C_6H_{12} flow (d, e and f). The spectra are reported by subtracting the spectra of the wet N_2-saturated sample to that of the wet (H_2O) CO_2-saturated one (a, b and c) or wet (C_6H_{12}) CO_2-saturated one. The black and coloured curves represent the wet (H_2O/C_6H_{12}) N_2-saturated and wet (H_2O/C_6H_{12}) CO_2-saturated samples, respectively. The curves of intermediate CO_2 coverages are shown in grey. The spectra were normalized by the underlying area of the structural interlayer carbonates (Fig. S5).

the intense HOH bending mode at 1640 cm^{-1}, a different solvent was used.

Even though water was chosen as the solvent closest to the reaction conditions, to further investigate the formation of carbonates upon CO_2 adsorption, the same tests were repeated in C_6H_{12} (experimental procedure reported in Section 2.2 and Fig. 4d-f).

The three samples show a carbonates spectral evolution coherent with what was previously observed for CO_2-saturated H_2O flow (see comparison in Figure S8) but with a higher spectral resolution. The IR spectra collected in C_6H_{12} are characterized by a band at 1448 cm^{-1} ascribed to the CH_2 scissoring bending mode [54]. However, considering the medium-weak intensity of this signal, it does not preclude the investigation of the carbonates spectral region. As previously observed in H_2O, upon contact with CO_2-saturated C_6H_{12} flow, the spectrum of Zn-Al 1:2 sample (Fig. 4d) shows an increase of the band at ~1340 cm^{-1} along with an increment of the signals in the 1700–1600 cm^{-1} range, now clearly displaying the presence of two distinct and well-resolved components at 1616 cm^{-1} and 1660 cm^{-1}. The band at 1340 cm^{-1} is characterized by a tail at low frequencies, confirming the existence of an additional component. The 1600–1370 cm^{-1} region also gradually increases in intensity, revealing the presence of two distinct components, although the presence of the CH_2 bending mode prevents a clear identification of the maxima. Similarly, Zn-Al 1:1 shows a first increase of the bands at 1616 and 1340 cm^{-1} followed by the increment of the bands at 1660 cm^{-1}. The latter can probably be coupled with a component falling between 1340 and 1200 cm^{-1}, as suggested by the asymmetric shape of the band with apparent maximum at 1340 cm^{-1}. An increase of the bands in the 1600–1370 cm^{-1} spectral region is also observed, although less pronounced than in Zn-Al 1:2. Lastly, the Zn-Al 2:1 spectrum is characterized by a scarce evolution of the carbonates bands.

For all samples, a spectral minimum at 1363 cm^{-1} was detected, but less pronounced than that observed in the water stream, suggesting a higher stability of the sample deposition when in contact with a C_6H_{12} solution.

By looking at the whole carbonate spectral profile, Zn-Al 1:2 displays a greater carbonates evolution than Zn-Al 1:1 and Zn-Al 2:1 in both H_2O and in C_6H_{12}. Interestingly, this result agrees with the volumetry data collected at 308 K, where Zn-Al 1:2 LDH shows a CO_2 capture capacity at 1 bar higher than for Zn-Al 1:1 and Zn-Al 2:1 (50% and 75% respectively). Another interesting finding is the possibility to better appreciate the existence of two IR components when the experiment is carried out in C_6H_{12} flow: one with an apparent maximum at 1660 cm^{-1} and another between 1340 and 1200 cm^{-1}, which were weakly detectable in the tests performed in H_2O. These bands can be associated to a basic oxygen, which preferentially interacts with H_2O rather than CO_2. For this reason, the interactions with these sites are only distinguishable when the experiments are carried out in C_6H_{12}. It is worth noting that the increase of those new spectral components is associated with a decrease of the signals in the 1580–1370 cm^{-1} range, suggesting that a family of carbonates forms at the expense of another.

After the spectroscopic study of the interaction of the CO_2-saturated H_2O and C_6H_{12} flows with the three samples (Fig. 4), the main carbonate-like species generated by CO_2 adsorption were tentatively assigned (Fig. 5 and Figure S9 and section S6 for the fit parameters). A fit of the main families of carbonates was performed, keeping the position of the structural interlayer H_2O and CO_3^{2-} components fixed (see Figure S5 and Figure S9 for the resulting fit and section S6 for the fit parameters in the SI).

As reported above, CO_2 can interact with basic sites or acid-base couples forming carbonate-like species, whose main signals are detected in the 1800–1200 cm^{-1} spectral range and originate from the decoupling of the original ν_3 asymmetric CO_3^{2-} signal at 1415 cm^{-1}, related to the free carbonate ion, into two stretching bands (symmetric and asymmetric carbonate components) [51]. The distance between those two "new" stretching components ($\Delta\nu_3$) is usually inversely proportional to the basic strength of the sites available in the material. Indeed, the monodentate carbonates, which have low coordination oxygen anions and account for the strongest basic sites, usually display a

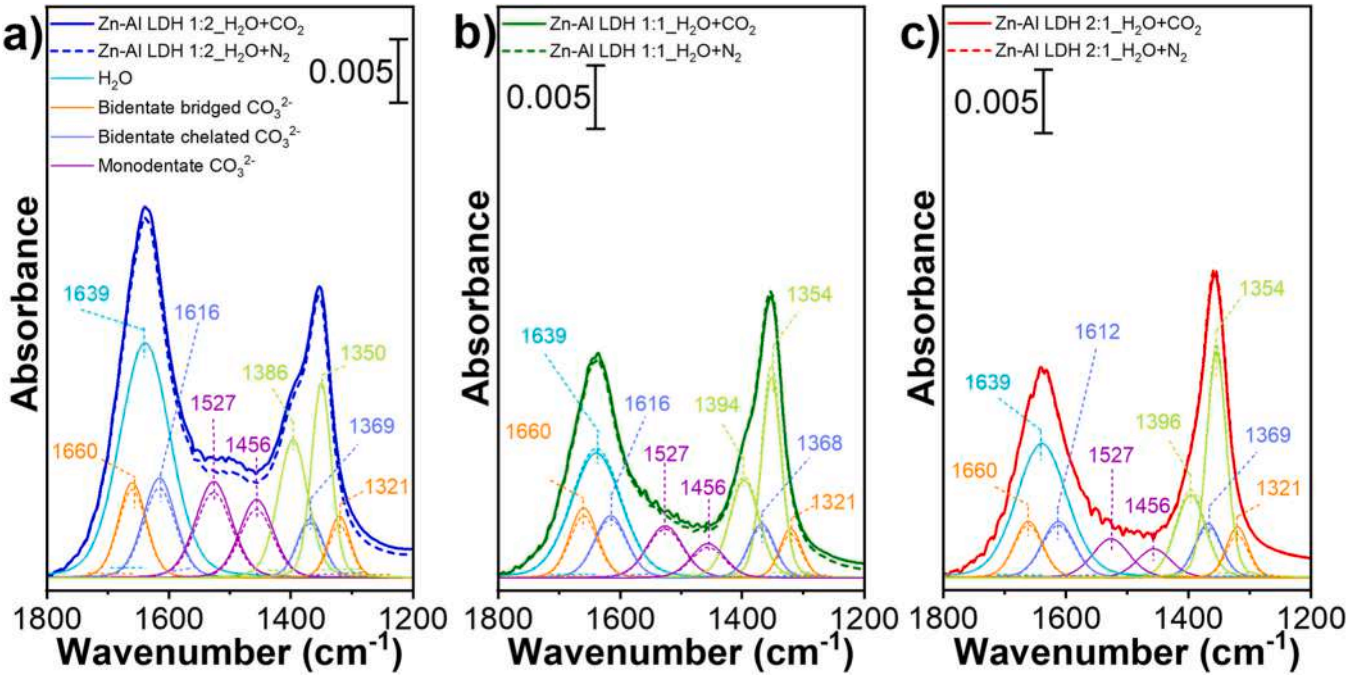

Fig. 5. Band fitting of carbonate-like species species of IR spectra collected under N_2-saturated and CO_2-saturated H_2O flows in the 1800–1200 cm^{-1} range. The spectral components of distinct carbonates species are evidenced by different colours: orange - Bidentate bridges (Bb), indigo - Bidentate chelated (Bc) and violet - Monodentate (M). The dashed curves refer to the spectrum and relative components of the wet N_2-saturated sample, while the solid curves refer to the spectrum and relative components of the wet CO_2-saturated samples (i.e the maximum CO_2 loading reached after 30 minutes). The components of asymmetrical vibration of structural carbonates are reported in light green and the component of bending vibrations of structural and physiosorbed water is reported in light blue. The resulting fit is reported in Fig. S9 and in section S6 for fit parameters.

$\Delta\nu_3$ of ~100 cm^{-1}. The bidentate carbonate-like species, which form on acid–base pairs (Zn^{2+}-O^{2-} or Al^{3+}-O^{2-}) and constitute the intermediate strength basic sites, usually show a $\Delta\nu_3$ of ~300 cm^{-1} for the chelated ones and of ~400 cm^{-1} for the bridged ones (see Table S3 for a sketch of the different carbonate-like species)) [30,34,51,53]. Lastly, the other carbonates can form upon CO_2 interaction as bicarbonates or polydentate species. Bicarbonates are easily discernible due to the presence of the characteristic, sharp C-OH bending (δ_{OH}) mode in the 1225–1240 cm^{-1} spectral range and are usually weakly bonded, while polydentate species in gas phase are usually strongly resistant to degassing conditions [51,55].

The assignment of carbonate species based on $\Delta\nu_3$ is not always straightforward, since the band frequencies can be affected by the polarizing power of the metal cations, the composition of the material, the presence of water and/or cations external to the metal coordination sphere, and many other factors [51,56,57]. However, the identification of the main carbonate species formed on LDHs reported in the literature is reasonable following the values of $\Delta\nu_3$ reported above (See Table S2) [31–34,58,59]. Di Cosimo et al. [31], who investigated the interaction of CO_2 with Mg-Al mixed oxides having different molar ratios (0.5–9.0), reported the presence of unidentate carbonates at 1510–1560 cm^{-1}(asym νO-C-O) and at 1360–1400 cm^{-1} (sym νO-C-O) with a $\Delta\nu_3$ in the range of 200–110 cm^{-1}. The bidentate carbonates were detected at 1630–1610 cm^{-1}(asym νO-C-O) and at 1340–1320 cm^{-1}(sym νO-C-O) with a $\Delta\nu_3$ of 310–270 cm^{-1}, while bicarbonate species show two bands at 1650 cm^{-1} and at 1480 cm^{-1} together with the appearance of the C-OH bending mode at 1220 cm^{-1}. Comparable frequencies were reported in a similar system by León et al. [32] where, unlike to Di Cosimo et al., two different families of unidentate carbonates and both chelated and bridged bidentate species were detected. Perez-Ramirez et al. [33] reported the presence of monodentate and bidentate chelated carbonates having a $\Delta\nu_3$ lower than the previously mentioned authors, while Coenen et al. [34], who investigated a K promoted Mg-Al mixed oxide in the presence of wet CO_2, mainly reported the appearance of bidentate species. Although the literature data reported above could be a good starting point for the assignment in this paper, all of them deal with the study of the carbonates formation in the gas phase on pre-calcined LDH samples, and are therefore far from the conditions reported here (contact with a CO_2 saturated liquid phase). To develop a consistent identification of the carbonate bands of this work, a correlation between the evolution of the bands observed upon CO_2 contact in both H_2O and C_6H_{12} was found (Fig. 4).

Consequently, the main bands have been assigned, mainly referring to the work of Debecker et al. [30], in the following way: (i) signals at 1527/1456 cm^{-1} to asymmetric and symmetric O-C-O stretching of monodentate carbonates (Md), (ii) components at 1616–1612/1368–1369 cm^{-1} to asymmetric and symmetric O-C-O stretching of bidentate chelated (Bc) carbonate and (iii) bands at 1660–1321 cm^{-1} to asymmetric and symmetric O-C-O stretching of bridged (Bb) carbonates. The absence of the characteristic δ_{OH} in the 1225–1240 cm^{-1} spectral range suggests the non-presence of bicarbonates even if the presence of the liquid phase complicates their identifications [60]. This assignment agrees with the bands evolution observed in the differential spectra (Fig. 4a-c). In particular, the couple of bands assigned to Md carbonates (orange components at 1527 and 1456 cm^{-1} in the band fitting of Fig. 5) exhibits a similar spectral behaviour in the differential spectra, which in contrast, differs from the evolution of the components associated with Bc carbonates (indigo signals at 1616–1612 and 1368–1369 cm^{-1} in the band fitting of Fig. 5). The Bb carbonates bands (violet bands at 1660 and 1321 cm^{-1} in the band fitting of Fig. 5) are in the same position at which new components were observed in the C_6H_{12} tests. It is worth recalling that the same signals were hardly detected in the presence of H_2O. This is consistent with the fact that bidentate carbonates formation requires a coordination vacancy to be available in the same coordination sphere of a basic oxygen. This circumstance is favoured only at higher degree of dehydration [55].

As previously pointed out, due to the low intensity of the signals, the carbonate evolution in the samples could be noticed only by subtracting the spectra of the wet N_2-saturated sample from the wet CO_2-saturated one. Indeed, the not-subtracted ATR-IR spectra show only few differences in the intensity of the various components (see difference between solid and dashed spectra in the whole range of Fig. 5). To better appreciate the evolution of the carbonate species over time, the band fitting of the spectra at intermediate CO_2 coverage (collected each 7.5 minutes after the switch of N_2 to CO_2) was performed and the area of the different carbonates spectral components was evaluated (Fig. 6 and Table 1). Even if a comparison of the carbonates evolution among the three samples would probably lead to a wrong interpretation, the change over time within the same sample could be better evaluated. In particular, contrary to what is observed in the other two LDHs, the Zn-Al 1:2 LDH shows a higher amount of Md carbonates compared to Bb and Bc. However, the sum of bidentate species (Bb+Bc) it is always higher than the Md carbonates in all samples. For this reason, to really highlight the differences among the various LDHs in carbonate species formed upon CO_2 interaction, an evaluation of the monodentate to total bidentate carbonates ratio (Md/(Bb+Bc)) must be carried out. Interestingly, the Md/(Bb+Bc) ratio of Zn-Al 1:2 is higher than for the other two samples (0.680 for Zn-Al 1:2 LDH versus 0.466 and 0.416 for Zn-Al 1:1 and 2:1 respectively), testifying a larger contribution of monodentate species in Zn-Al 1:2. By looking at the bidentate species individually, all samples show a higher content of Bc species compared to the Bb carbonates (Bb/Bc ratio of 0.840, 0.857 and 0.811 in Zn-Al 1:2, 1:1 and 2:1, respectively).

With the same criteria, the band fitting was performed to the experiments performed in C_6H_{12} (Figure S10 and Figure S11 and Section 6 for the fit parameters), showing a behavior comparable to the one observed in the presence of water. Even if the ratios of the intensity of the different carbonate components are different compared to the test in water, the amount of carbonate-like species, and in particular of Md carbonates, of the Zn-Al 1:2 sample is significantly higher than for the other two LDHs (Table S4).

Since the different carbonate species are strictly connected with the strength of the basic sites, the relative intensities of the IR bands of the various carbonates families provides a powerful tool to discriminate among materials with different basic nature. In particular, the prevalence of the Md carbonates in Zn-Al 1:2 is probably related to the presence of a higher content of low coordination oxygen anions having a strong basic character. On the other hand, Zn-Al 1:1 and 2:1, with a lower Md/(Bb+Bc) ratio, are probably characterized by a higher content of acid–base pairs with intermediate basic strength. Interestingly, Zn-Al 1:2 also exhibits a more pronounced difference between the spectra of the CO_2-saturated and N_2-saturated sample, (see solid and dashed spectra of Fig. 5a in the whole range), together with a higher CO_2 adsorption capacity displayed in the volumetric measurements (Figure S3). Those results ultimately suggest not only the presence of stronger basic sites in Zn-Al 1:2, but also an overall higher affinity of this sample towards CO_2.

The different basic sites are expected to play a crucial role in the overall reaction during the electrocatalytic tests. For this reason, the results derived from the spectroscopic investigation of the different species involved in the CO_2 interaction could explain the highest performances of Zn-Al 1:2 in the CO2RR.

4. Conclusion

In this work, three different Zn-Al LDHs having a Zn^{2+}/Al^{3+} ratio of 2.0, 1.0 and 0.50 were synthesized by means of a co-precipitation method and characterized. The possible applicability of those materials for the electrochemical CO2RR to CO was tested in a custom-made three-compartment cell, using $KHCO_3$ as electrolytic solution. The two

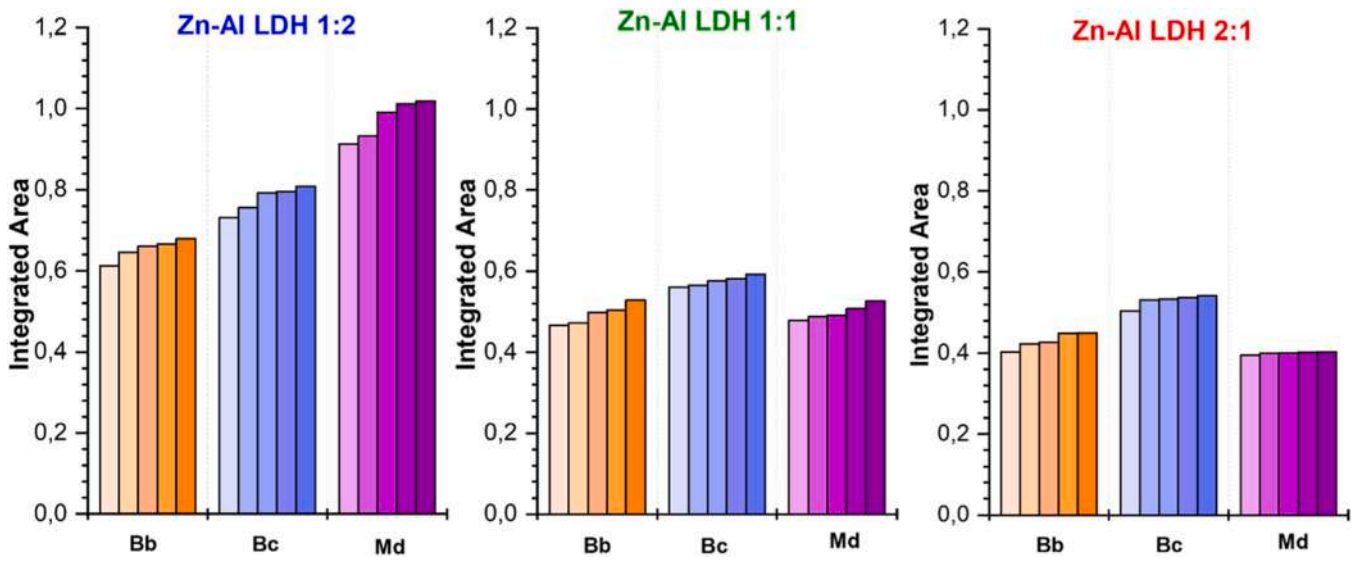

Fig. 6. Evolution of the carbonate species over time. The band fitting of the spectra at intermediate CO_2 coverage (0,7.5,15, 22.5, 30 minutes) was performed (as reported in Fig. 5 for the 0 and 30 minutes coverage) and the area of the carbonates components was evaluated by summing the asymmetric and the symmetric contributions of the same carbonate species. The numbers reported are normalized to the area of the fit of the interlayer carbonates.

Table 1
Evaluation of the carbonate species formed upon the interaction of the samples with a CO_2-saturated H_2O flow. For each sample, the average of the intensities of the histograms in Fig. 6 (Average), the sum of bridged and chelated bidentate (Total Bidentate Bb+Bc), the Monodentate to Bidentate ratio (Md/Bb+Bc) and the ratio between the two bidentate species (Bb/Bc) was reported.

	Carbonate species	Average	Bb+Bc	Md/(Bb+Bc)	Bb/Bc
Zn-Al LDH 1:2	Bidentate bridged (Bb)	0.652	1.430	0.680	0.840
	Bidentate chelated (Bc)	0.776			
	Monodentate (Md)	0.973			
Zn-Al LDH 1:1	Bidentate bridged (Bb)	0.493	1.069	0.466	0.857
	Bidentate chelated (Bc)	0.575			
	Monodentate (Md)	0.498			
Zn-Al LDH 2:1	Bidentate bridged (Bb)	0.429	0.959	0.416	0.811
	Bidentate chelated (Bc)	0.529			
	Monodentate (Md)	0.399			

major products formed during the reaction were CO and H_2, which are competitively generated. The selectivity for CO increased by reducing the Zn/Al ratio at the expense of H_2 which progressively decreased till reaching, for Zn-Al LDH 1:2, a selectivity of 40% for CO and of 42% for H_2, under the applied potential of 1.4 V vs. RHE.

To investigate the active sites and their evolution upon a CO_2-saturated liquid flow, an extensive ATR-IR spectroscopic characterization was performed. Firstly, the as-synthesized dried samples depositions were studied by means of IR and Raman spectroscopy, confirming the presence of the vibrational modes usually associated with the hydrotalcite structure. The CO_2 affinity was also evaluated by means of volumetric adsorption measurements, showing, for Zn-Al 2:1 LDH, the highest capture capacity (0.36 mmol g^{-1} at 308 K and 1 bar).

Afterwards, the evolution of the IR bands of samples in interaction with a CO_2-saturated H_2O flow was investigated, showing peculiar differences in the 1800–1200 cm^{-1} spectral region, possibly associated with the formation of different carbonate families. The same experiment was also repeated using C_6H_{12} as a solvent, so reducing the deposition loss and allowing the discrimination of the different IR components. By considering the evolution of the carbonate bands upon CO_2 interaction in both H_2O and C_6H_{12}, and by comparing them with the literature data, the signals ascribed to the different carbonates families were easily identified. Looking at the ratio between Md carbonates and bidentate one (Md/(Bb+Bc)), the Zn-Al 1:2 LDH shows a greater contribution of monodentate species with respect to the others.

The differences observed in the carbonate families provides a powerful tool to discriminate among materials with different basic sites. Considering the Zn-Al 1:2 LDH, where the Md carbonates prevail, a higher content of low coordination oxygen anions with strong basic character is expected. On the other hand, increasing the Zn^{2+}/Al^{3+} ratio, the samples are characterized by a higher content of acid-base pairs with intermediate basic strength. Since the CO_2 adsorption is the first step of the CO2RR, differences in the basic character and, consequently, in the carbonate formation are expected to play a crucial role in the overall reaction. In addition, since the spectroscopic characterization was carried out without any previous treatment of the samples, the present work could be useful for the study of adsorption processes under more realistic conditions, since, to the best of our knowledge, this is the only work dealing with the study of CO_2 adsorption on LDHs in a water environment.

CRediT authorship contribution statement

Silvia Bordiga: Writing – review & editing, Visualization, Validation, Supervision, Methodology, Funding acquisition. **Joke Hadermann:** Writing – review & editing, Visualization, Validation, Supervision, Resources, Project administration, Methodology, Funding acquisition, Data curation, Conceptualization. **Kiyoharu Tadanaga:** Writing – review & editing, Visualization, Validation, Supervision, Resources, Project administration, Methodology, Funding acquisition, Data curation, Conceptualization. **Nataly Carolina Rosero-Navarro:** Writing – review & editing, Visualization, Validation, Supervision, Resources, Project administration, Methodology, Investigation, Funding acquisition, Conceptualization. **Natale Gabriele Porcaro:** Writing – review & editing, Visualization, Validation, Supervision, Methodology, Investigation, Formal analysis, Data curation, Conceptualization. **Ryosuke Nakazato:** Writing – original draft, Visualization, Methodology, Investigation, Formal analysis, Data curation. **Matthias Quintelier:** Writing – original draft, Visualization, Validation, Methodology,

Investigation, Formal analysis, Data curation. **Matteo Signorile:** Writing – review & editing, Visualization, Validation, Supervision, Methodology, Data curation, Conceptualization. **Valentina Crocellà:** Writing – review & editing, Visualization, Validation, Supervision, Methodology, Investigation, Conceptualization, Funding acquisition. **Melodj Dosa:** Writing – original draft, Visualization, Methodology, Investigation, Formal analysis, Data curation. **Francesca Bonino:** Writing – review & editing, Visualization, Validation, Supervision, Resources, Project administration, Methodology, Funding acquisition, Conceptualization. **Margherita Cavallo:** Writing – review & editing, Writing – original draft, Visualization, Validation, Methodology, Investigation, Formal analysis, Data curation, Conceptualization.

Declaration of Competing Interest

The authors declare that they have no known competing financial interests or personal relationships that could have appeared to influence the work reported in this paper.

Data Availability

Data will be made available on request.

Acknowledgements

This work was supported by 4AirCRAFT project under the strategic international cooperation between Europe and Japan. 4AirCRAFT has received funding from the European Union's Horizon 2020 research and innovation programme (No 101022633) and Japan Science and Technology Agency (JST) (No JPMJSC2102). We acknowledge the Hercules fund 'Direct electron detector for soft matter TEM' from Flemish Government for the purchase of the K2 DED. MC, MD, NGP, MS, SB, VC and FB acknowledge support from the Project CH4.0 under the MUR program "Dipartimenti di Eccellenza 2023–2027" (CUP: D13C22003520001)

Appendix A. Supporting information

Supplementary data associated with this article can be found in the online version at doi:10.1016/j.jcou.2024.102804.

References

[1] P. Friedlingstein, M. O'sullivan, M.W. Jones, R.M. Andrew, L. Gregor, J. Hauck, C. Le Quéré, I.T. Luijkx, A. Olsen, G.P. Peters, W. Peters, J. Pongratz, C. Schwingshackl, S. Sitch, J.G. Canadell, P. Ciais, R.B. Jackson, S.R. Alin, R. Alkama, A. Arneth, V.K. Arora, N.R. Bates, M. Becker, N. Bellouin, H.C. Bittig, L. Bopp, F. Chevallier, L.P. Chini, M. Cronin, W. Evans, S. Falk, R.A. Feely, T. Gasser, M. Gehlen, T. Gkritzalis, L. Gloege, G. Grassi, N. Gruber, Ö. Gürses, I. Harris, M. Hefner, R.A. Houghton, G.C. Hurtt, Y. Iida, T. Ilyina, A.K. Jain, A. Jersild, K. Kadono, E. Kato, D. Kennedy, K. Klein Goldewijk, J. Knauer, J. I. Korsbakken, P. Landschützer, N. Lefèvre, K. Lindsay, J. Liu, Z. Liu, G. Marland, N. Mayot, M.J. Mcgrath, N. Metzl, N.M. Monacci, D.R. Munro, S.I. Nakaoka, Y. Niwa, K. O'brien, T. Ono, P.I. Palmer, N. Pan, D. Pierrot, K. Pocock, B. Poulter, L. Resplandy, E. Robertson, C. Rödenbeck, C. Rodriguez, T.M. Rosan, J. Schwinger, R. Séférian, J.D. Shutler, I. Skjelvan, T. Steinhoff, Q. Sun, A.J. Sutton, C. Sweeney, S. Takao, T. Tanhua, P.P. Tans, X. Tian, H. Tian, B. Tilbrook, H. Tsujino, F. Tubiello, G.R. Van Der Werf, A.P. Walker, R. Wanninkhof, C. Whitehead, A. Willstrand Wranne, R. Wright, W. Yuan, C. Yue, X. Yue, S. Zaehle, J. Zeng, B. Zheng, Global Carbon Budget 2022, Earth Syst. Sci. Data 14 (2022) 4811–4900, https://doi.org/10.5194/ESSD-14-4811-2022.

[2] H. Lee, K. Calvin, D. Dasgupta, …, G. Krinner, CLIMATE CHANGE 2023 Synthesis Report Summary for Policymakers, (2023). ⟨https://ntrs.nasa.gov/citations/20230009518⟩ (accessed November 3, 2023).

[3] C. Faber, Y. Allahverdiyeva-Rinne, V. Artero, L. Baraton, A. Barbieri, H. Bercegol, M. Fleischer, H. Huynhthi, J. Kargul, H. Lepaumier, L. López, A. Magnuson, A. Roth, Deliverable 1.2. ROADMAP TECHNICAL APPENDIX. Part 4 - Sustainable Carbon Capture and SUNRISE Key Enablers, Sunr. Sol. Energy a Circ. Econ. (2019) 1–95, https://doi.org/10.5281/ZENODO.3923437.

[4] M. Mikkelsen, M. Jørgensen, F.C. Krebs, The teraton challenge. A review of fixation and transformation of carbon dioxide, Energy Environ. Sci. 3 (2010) 43–81, https://doi.org/10.1039/B912904A.

[5] G. Centi, E.A. Quadrelli, S. Perathoner, Catalysis for CO_2 conversion: a key technology for rapid introduction of renewable energy in the value chain of chemical industries, Energy Environ. Sci. 6 (2013) 1711–1731, https://doi.org/10.1039/C3EE00056G.

[6] B. Kumar, M. Llorente, J. Froehlich, T. Dang, A. Sathrum, C.P. Kubiak, Photochemical and Photoelectrochemical Reduction of CO_2, Https://Doi.Org/10.1146/Annurev-Physchem-032511-143759 63 (2012) 541–569. ⟨https://doi.org/10.1146/ANNUREV-PHYSCHEM-032511-143759⟩.

[7] Q. Lu, F. Jiao, Electrochemical CO_2 reduction: electrocatalyst, reaction mechanism, and process engineering, Nano Energy 29 (2016) 439–456, https://doi.org/10.1016/J.NANOEN.2016.04.009.

[8] H.R.M. Jhong, S. Ma, P.J. Kenis, Electrochemical conversion of CO_2 to useful chemicals: current status, remaining challenges, and future opportunities, Curr. Opin. Chem. Eng. 2 (2013) 191–199, https://doi.org/10.1016/J.COCHE.2013.03.005.

[9] R. Kortlever, J. Shen, K.J.P. Schouten, F. Calle-Vallejo, M.T.M. Koper, Catalysts and reaction pathways for the electrochemical reduction of carbon dioxide, J. Phys. Chem. Lett. 6 (2015) 4073–4082, https://doi.org/10.1021/ACS.JPCLETT.5B01559/ASSET/IMAGES/MEDIUM/JZ-2015-01559C_0005.GIF.

[10] S. Jin, Z. Hao, K. Zhang, Z. Yan, J. Chen, Advances and challenges for the electrochemical reduction of CO_2 to CO: from fundamentals to industrialization, Angew. Chem. 133 (2021) 20795–20816, https://doi.org/10.1002/ANGE.202101818.

[11] X. Zhang, S.X. Guo, K.A. Gandionco, A.M. Bond, J. Zhang, Electrocatalytic carbon dioxide reduction: from fundamental principles to catalyst design, Mater. Today Adv. 7 (2020) 100074, https://doi.org/10.1016/J.MTADV.2020.100074.

[12] Y. Wang, D. He, H. Chen, D. Wang, Catalysts in electro-, photo- and photoelectrocatalytic CO_2 reduction reactions, J. Photochem. Photobiol. C: Photochem. Rev. 40 (2019) 117–149, https://doi.org/10.1016/J.JPHOTOCHEMREV.2019.02.002.

[13] L. Lu, Y. Zheng, R. Yang, A. Kakimov, X. Li, Recent advances of layered double hydroxides–based bifunctional electrocatalysts for ORR and OER, Mater. Today Chem. 21 (2021) 100488, https://doi.org/10.1016/J.MTCHEM.2021.100488.

[14] S. Anantharaj, K. Karthick, S. Kundu, Evolution of layered double hydroxides (LDH) as high performance water oxidation electrocatalysts: a review with insights on structure, activity and mechanism, Mater. Today Energy 6 (2017) 1–26, https://doi.org/10.1016/J.MTENER.2017.07.016.

[15] H. Kowsari, M. Mehrpooya, F. Pourfayaz, Nitrogen and sulfur doped ZnAl layered double hydroxide/reduced graphene oxide as an efficient nanoelectrocatalyst for oxygen reduction reactions, Int J. Hydrog. Energy 45 (2020) 27129–27144, https://doi.org/10.1016/J.IJHYDENE.2020.07.068.

[16] J. Pérez-Ramírez, S. Abelló, N.M. Van Der Pers, Memory effect of activated Mg–Al hydrotalcite: In Situ XRD studies during decomposition and gas-phase reconstruction, Chem. – A Eur. J. 13 (2007) 870–878, https://doi.org/10.1002/CHEM.200600767.

[17] T. Baskaran, J. Christopher, A.S.-R. Advances, undefined 2015, Progress on layered hydrotalcite (HT) materials as potential support and catalytic materials, Pubs.Rsc.orgT Baskaran, J Christopher, A SakthivelRsc Advances, 2015•pubs.Rsc.Org (n.d.). ⟨https://pubs.rsc.org/en/content/articlehtml/2015/ra/c5ra19909c?casa_token=24VKli2HwmoAAAAA:yDDBWxW3b3_WdIkPY6HuYqujCqABN2rLs9zR5dKGfrhIKL20HLOPdXQLfQOkTHl6wt3sOrg6Sltx0g⟩ (Accessed November 3, 2023).

[18] Y. Arishige, D. Kubo, K. Tadanaga, A. Hayashi, M. Tatsumisago, Electrochemical oxygen separation using hydroxide ion conductive layered double hydroxides, Solid State Ion.-. 262 (2014) 238–240, https://doi.org/10.1016/J.SSI.2013.09.009.

[19] K. Tadanaga, Y. Furukawa, A. Hayashi, M. Tatsumisago, Direct ethanol fuel cell using hydrotalcite clay as a hydroxide ion conductive electrolyte, Adv. Mater. 22 (2010) 4401–4404, https://doi.org/10.1002/ADMA.201001766.

[20] L. Tan, Z. Wang, Y. Zhao, Y.F. Song, Recent progress on nanostructured layered double hydroxides for visible-light-induced photoreduction of CO_2, Chem. Asian J. 15 (2020) 3380–3389, https://doi.org/10.1002/ASIA.202000963.

[21] J. Zhang, J. Liu, L. Xi, Y. Yu, N. Chen, S. Sun, W. Wang, K.M. Lange, B. Zhang, Single-atom Au/NiFe layered double hydroxide electrocatalyst: probing the origin of activity for oxygen evolution reaction, J. Am. Chem. Soc. 140 (2018) 3876–3879, https://doi.org/10.1021/JACS.8B00752/SUPPL_FILE/JA8B00752_SI_001.PDF.

[22] Z. Lu, W. Xu, W. Zhu, Q. Yang, X. Lei, J. Liu, Y. Li, X. Sun, X. Duan, Three-dimensional NiFe layered double hydroxide film for high-efficiency oxygen evolution reaction, Chem. Commun. 50 (2014) 6479–6482, https://doi.org/10.1039/C4CC01625D.

[23] M. Gong, Y. Li, H. Wang, Y. Liang, J.Z. Wu, J. Zhou, J. Wang, T. Regier, F. Wei, H. Dai, An advanced Ni-Fe layered double hydroxide electrocatalyst for water oxidation, J. Am. Chem. Soc. 135 (2013) 8452–8455, https://doi.org/10.1021/JA4027715/SUPPL_FILE/JA4027715_SI_001.PDF.

[24] P. Zhai, M. Xia, Y. Wu, G. Zhang, J. Gao, B. Zhang, S. Cao, Y. Zhang, Z. Li, Z. Fan, C. Wang, X. Zhang, J.T. Miller, L. Sun, J. Hou, Engineering single-atomic ruthenium catalytic sites on defective nickel-iron layered double hydroxide for overall water splitting, 2021 12:1 12, Nat. Commun. (2021) 1–11, https://doi.org/10.1038/s41467-021-24828-9.

[25] K. Iwase, T. Hirano, I. Honma, Copper aluminum layered double hydroxides with different compositions and morphologies as electrocatalysts for the carbon dioxide reduction reaction, ChemSusChem 15 (2022) e202102340, https://doi.org/10.1002/CSSC.202102340.

[26] M. Serafini, F. Mariani, A. Fasolini, E.T. Brandi, E. Scavetta, F. Basile, D. Tonelli, Electrosynthesized CuMgAl layered double hydroxides as new catalysts for the

electrochemical reduction of CO2, Adv. Funct. Mater. 33 (2023) 2300345, https://doi.org/10.1002/ADFM.202300345.
[27] N. Yamaguchi, R. Nakazato, K. Matsumoto, M. Kakesu, N.C. Rosero-Navarro, A. Miura, K. Tadanaga, Electrocatalytic property of Zn-Al layered double hydroxides for CO_2 electrochemical reduction, J. Asian Ceram. Soc. 11 (2023) 406–411, https://doi.org/10.1080/21870764.2023.2236441.
[28] R. Nakazato, K. Matsumoto, N. Yamaguchi, M. Cavallo, V. Crocellà, F. Bonino, M. Quintelier, J. Hadermann, N.C. Rosero-Navarro, A. Miura, K. Tadanaga, CO_2 Electrochemical reduction with Zn-Al layered double hydroxide-loaded gas-diffusion electrode, Electrochemistry (2023), https://doi.org/10.5796/ELECTROCHEMISTRY.23-00080.
[29] H. Wang, Y.W. Zhou, W.Bin Cai, Recent applications of in situ ATR-IR spectroscopy in interfacial electrochemistry, Curr. Opin. Electrochem 1 (2017) 73–79, https://doi.org/10.1016/J.COELEC.2017.01.008.
[30] D.P. Debecker, E.M. Gaigneaux, G. Busca, Exploring, tuning, and exploiting the basicity of hydrotalcites for applications in heterogeneous catalysis, Chem. A Eur. J. 15 (2009) 3920–3935, https://doi.org/10.1002/CHEM.200900060.
[31] J.I. Di Cosimo, V.K. Díez, M. Xu, E. Iglesia, C.R. Apesteguía, Structure and Surface and Catalytic Properties of Mg-Al Basic Oxides, 1998.
[32] M. León, E. Díaz, S. Bennici, A. Vega, S. Ordóñez, A. Auroux, Adsorption of CO_2 on hydrotalcite-derived mixed oxides: sorption mechanisms and consequences for adsorption irreversibility, Ind. Eng. Chem. Res 49 (2010) 3663–3671, https://doi.org/10.1021/ie902072a.
[33] J. Pérez-RamÍrez, G. Mul, J.A. Moulijn, In situ Fourier transform infrared and laser Raman spectroscopic study of the thermal decomposition of Co-Al and Ni-Al hydrotalcites, 2001.
[34] K. Coenen, F. Gallucci, B. Mezari, E. Hensen, M. van Sint Annaland, An in-situ IR study on the adsorption of CO_2 and H_2O on hydrotalcites, J. CO2 Util. 24 (2018) 228–239, https://doi.org/10.1016/J.JCOU.2018.01.008.
[35] D. Ferri, T. Biirgi, A. Baiker, Pt and Pt/Al2O3 Thin films for investigation of catalytic solid−liquid interfaces by ATR-IR spectroscopy: CO adsorption, H_2-induced reconstruction and surface-enhanced absorption, J. Phys. Chem. B 105 (2001) 3187–3195, https://doi.org/10.1021/JP002268I.
[36] M. Grahn, A. Holmgren, J. Hedlund, Adsorption of n-Hexane and p-Xylene in thin silicalite-1 films studied by FTIR/ATR spectroscopy, J. Phys. Chem. C. 112 (2008) 7717–7724, https://doi.org/10.1021/JP800345V.
[37] A.J. McQuillan, Probing solid–solution interfacial chemistry with ATR-IR spectroscopy of particle films, Adv. Mater. 13 (2001) 1034–1038. ⟨https://onlinelibrary.wiley.com/doi/abs/10.1002/1521-4095(200107)13:12/13%3C1034::AID-ADMA1034%3E3.0.CO;2-7?casa_token=lZlGTAWkYIgAAAAA:5BgRdTVsBDcORAXDgKw8WZPvLU-sNsOXEdJ9-qlXYBYZOKAzlbDfgrPmD3xHgttkxuECrg3io5R7STE⟩ (Accessed November 3, 2023).
[38] T. Bürgi, M. Bieri, Time-resolved in situ ATR spectroscopy of 2-propanol oxidation over Pd/Al_2O_3: evidence for 2-propoxide intermediate, J. Phys. Chem. B 108 (2004) 13364–13369, https://doi.org/10.1021/JP048187U.
[39] R. Wirz, D. Ferri, A. Baiker, ATR-IR spectroscopy of pendant NH_2 groups on silica involved in the knoevenagel condensation, Langmuir 22 (2006) 3698–3706, https://doi.org/10.1021/LA053145Y/ASSET/IMAGES/MEDIUM/LA053145YN00001.GIF.
[40] X. Wu, J.W. Sun, P.F. Liu, J.Y. Zhao, Y. Liu, L. Guo, S. Dai, H.G. Yang, H. Zhao, Molecularly dispersed cobalt phthalocyanine mediates selective and durable CO_2 reduction in a membrane flow cell, Adv. Funct. Mater. 32 (2022), https://doi.org/10.1002/ADFM.202107301.
[41] M. Yasaei, M. Khakbiz, … A.Z. -M.S and, undefined 2019, Synthesis and characterization of Zn/Al-LDH@ SiO2 nanohybrid: Intercalation and release behavior of vitamin C, Elsevier (n.d.). ⟨https://www.sciencedirect.com/science/article/pii/S0928493118339699?casa_token=3vI912l5RuUAAAAA:gbSgTIqHtAWFL2mR90bnlxrMh07YnAsviEH20PMBy5Cus02RG-1hMa1AmDsWAb9w2AjJqCgHFg⟩ (Accessed November 3, 2023).
[42] A. Mujtaba, N.K. Janjua, Fabrication and electrocatalytic application of $CuO@Al_2O_3$ hybrids, J. Electrochem Soc. 162 (2015) H328–H337, https://doi.org/10.1149/2.0351506JES/XML.
[43] S. Khan, S. Shah, N. Janjua, A. Yurtcan, M.N.- Chemosphere, Alumina supported copper oxide nanoparticles (CuO/Al_2O_3) as high-performance electrocatalysts for hydrazine oxidation reaction, Chrommosphere 315 (2023) 137659. ⟨https://www.sciencedirect.com/science/article/pii/S0045653522041522⟩ (accessed January 31, 2024).
[44] S. Ng, C. Iffelsberger, J. Michalicka, M. Pumera, Atomic layer deposition of electrocatalytic insulator Al_2O_3 on three-dimensional printed nanocarbons, ACS Publ. 15 (2021) 686–697, https://doi.org/10.1021/acsnano.0c06961.
[45] H. Lei, Y. Liang, G. Cen, B.-T. Liu, S. Tan, Z. Wang, W. Mai, Atomic layer deposited Al_2O_3 layer confinement: an efficient strategy to synthesize durable MOF-derived catalysts toward the oxygen evolution reaction, Pubs. RSC Org. 8 (2021) 1432, https://doi.org/10.1039/d0qi01317j.
[46] Y. Zou, S. Xi, T. Bo, X. Zhou, J. Ma, X. Yang, Mesoporous amorphous Al_2O_3/crystalline WO_3 heterophase hybrids for electrocatalysis and gas sensing applications, J. Mater. (2021). ⟨https://pubs.rsc.org/en/content/articlehtml/2019/ta/c9ta08633a⟩ (accessed January 31, 2024).
[47] J.T. Kloprogge, R.L. Frost, Fourier transform infrared and Raman spectroscopic study of the local structure of Mg-, Ni-, and Co-hydrotalcites, J. Solid State Chem. 146 (1999) 506–515, https://doi.org/10.1006/JSSC.1999.8413.
[48] S. Miyata, The syntheses of hydrotalcite-like compounds and their structures and physico-chemical properties-i: the systems Mg^{2+}-Al^{3+}-NO_3, Mg^{2+}-Al^{3+}-Cl^-, Mg^{2+}-Al^{3+}-ClO_4^-, Ni^{2+}-Al^{3+}-Cl^- and Zn^{2+}-Al^{3+}-Cl^-, Clays Clay Min. 23 (1975) 369–375, https://doi.org/10.1346/CCMN.1975.0230508/METRICS.
[49] J. Liu, J. Song, H. Xiao, L. Zhang, Y. Qin, D. Liu, W. Hou, N. Du, Synthesis and thermal properties of ZnAl layered double hydroxide by urea hydrolysis, Powder Technol. 253 (2014) 41–45, https://doi.org/10.1016/J.POWTEC.2013.11.007.
[50] E. Alibakhshi, E. Ghasemi, M. Mahdavian, B. Ramezanzadeh, Corrosion Inhibitor Release from Zn-Al-$[PO_4^{3-}]$-$[CO_3^{2-}]$ Layered Double Hydroxide Nanoparticles, Prog. Color., Color. Coat. 9 (2016) 233–248, https://doi.org/10.30509/PCCC.2016.75889.
[51] G. Busca, V. Lorenzelli, Infrared spectroscopic identification of species arising from reactive adsorption of carbon oxides on metal oxide surfaces, Mater. Chem. 7 (1982) 89–126, https://doi.org/10.1016/0390-6035(82)90059-1.
[52] F.M. Labajos, V. Rives, M.A. Ulibarri, A FT-IR and V-UV Spectroscopic Study of Nickel-Containing Hydrotalcite-Like Compounds, $[Ni_{1-x}Al_x(OH)_2](CO_3)_{x/2}.nH_2O$, Https://Doi.Org/10.1080/00387019108018133 24 (2006) 499–508. ⟨https://doi.org/10.1080/00387019108018133⟩.
[53] S.J. Palmer, R.L. Frost, G. Ayoko, T. Nguyen, Synthesis and Raman spectroscopic characterisation of hydrotalcite with CO_3^{2-} and $(MoO_4)^{2-}$ anions in the interlayer, J. Raman Spectrosc. 39 (2008) 395–401, https://doi.org/10.1002/jrs.1838.
[54] H. Takahashi, T. Shimanouchi, K. Fukushima, T. Miyazawa, Infrared spectrum and normal vibrations of cyclohexane, J. Mol. Spectrosc. 13 (1964) 43–56, https://doi.org/10.1016/0022-2852(64)90053-0.
[55] C. Morterra, G. Ghiotti, F. Boccuzzi, S. Coluccia, Infrared Spectrosc. Investig. Surf. Prop. Magnes. Aluminate Spine1 (1978).
[56] R.E. Hester, W.E.L. Grossman, Vibrational Analysis of Bidentate Nitrate and Carbonate Complexes1, (n.d.). ⟨https://pubs.acs.org/sharingguidelines⟩ (Accessed July 4, 2023).
[57] J.P. Jolivet, Y. Thomas, B. Taravel, V. Lorenzelli, G. Busca, Infrared spectra of cerium and thorium pentacarbonate complexes, J. Mol. Struct. 79 (1982) 403–408, https://doi.org/10.1016/0022-2860(82)85091-6.
[58] H.A. Prescott, Z.J. Li, E. Kemnitz, A. Trunschke, J. Deutsch, H. Lieske, A. Auroux, Application of calcined Mg–Al hydrotalcites for Michael additions: an investigation of catalytic activity and acid–base properties, J. Catal. 234 (2005) 119–130, https://doi.org/10.1016/J.JCAT.2005.06.004.
[59] S. Walspurger, L. Boels, P.D. Cobden, G.D. Elzinga, W.G. Haije, R.W. Van Den Brink, The Crucial Role of the K^+–Aluminium Oxide Interaction in K^+-Promoted Alumina- and Hydrotalcite-Based Materials for CO_2 Sorption at High Temperatures, ChemSusChem 1 (2008) 643–650, https://doi.org/10.1002/CSSC.200800085.
[60] M. Signorile, D. Salusso, V. Crocellà, M.C. Paganini, S. Bordiga, F. Bonino, D. Ferri, Surface species in direct liquid phase synthesis of dimethyl carbonate from methanol and CO_2: an MCR-ALS augmented ATR-IR study, Phys. Chem. Chem. Phys. 25 (2023) 8392–8402, https://doi.org/10.1039/D2CP05800F.